

## **Chapter Two**

### **Experimental Techniques**

#### **2.1 Overview**

The growth of b-axis-oriented rare earths involves the extensive use of specialized tools for thin film growth and for determination of the properties. Equipment for these purposes is now well-developed and commercially available. These are nevertheless research tools that require training, and information is available in review articles, books, and theses. The present Chapter describes specific experimental processes relevant to the research presented in Chapter 3. The Chapter is organized as follows. First, the EpiCenter laboratory and the crystal growth systems used for b-axis-oriented rare earths are described. Next, experimental techniques used for surface characterization are addressed. These include in situ reflection high-energy electron diffraction (RHEED) and ex situ atomic force microscopy (AFM). Then techniques employed to characterize the 3D structure of thin films are discussed. These include x-ray diffraction (XRD) and Rutherford backscattering spectroscopy (RBS). The Chapter concludes with a description of equipment and procedures for the determination of magnetic properties using SQUID magnetometry.

#### **2.2 Thin Film Growth**

##### **Thin Film Growth Laboratory**

The thin films were synthesized in the University of Illinois EpiCenter, which contains equipment for molecular beam epitaxy. This laboratory comprises six MBE systems and a UHV chemical vapor deposition (CVD) system, interconnected by UHV transfer lines and housed in a class 1000 cleanroom. This system includes additional equipment that permits

thin film characterization by surface x-ray diffraction (SXRD), x-ray/ultraviolet photoelectron spectroscopy (XPS/UPS), and scanning tunneling microscopy (STM). The instruments all function with the same sample holders, so that thin films can be prepared and then studied in a common UHV environment. The laboratory was recently expanded to include equipment located in the room below, with a 1.5 MeV van de Graff accelerator for RBS, PIXE, etc., a fixed-tube x-ray diffractometer (XRD), and a low-energy electron microscope (LEEM). A plan of this laboratory is provided as Figure 2.1.

## Thin Film Growth Equipment

The samples were grown using two Perkin-Elmer 430 molecular beam epitaxy machines which were extensively modified, as shown in Figure 2.2. The primary pumping in each chamber is provided by a cryopump and an ion pump, and the additional Ti sublimation pump is essential for removing an N<sub>2</sub> contaminant during high-temperature outgassing of substrates. One chamber was used for this sample outgassing and for electron-beam deposition on sapphire of the initial Ta buffer layer. The pressure rose from below  $1 \times 10^{-10}$  torr to  $1 \times 10^{-9}$  torr during this process, due to H<sub>2</sub> released during Ta evaporation. Samples were subsequently cooled to room temperature and moved through the UHV transfer tube into the second growth chamber for completion. The transfer usually took about four minutes at a pressure below  $1 \times 10^{-9}$  torr. After transfer the fresh Ta buffer layer was outgassed again above the final growth temperature of about 600 °C for several hours.

Dy was obtained from a Knudsen-type evaporation cell using a pyrolytic boron nitride crucible. Lu and Y fluxes were both obtained by evaporation from high-temperature (1700 °C) Knudsen-type evaporation cells, using Ta-lined, TaC-coated graphite crucibles. Ta has a small solubility in the rare earths at high temperature, but a Ta contaminant was never detected in the residual gas analysis (RGA) spectrum or with RBS [1]. The poor efficiency of the high-temperature Knudsen cells, which required nearly 1.5 kW per cell to achieve adequate flux, caused heating of the source flange and boiling of liquid nitrogen in the cryoshroud. Eventually, the thermal stress caused a vacuum leak and the problem was finally overcome by using water rather than liquid nitrogen as a coolant.

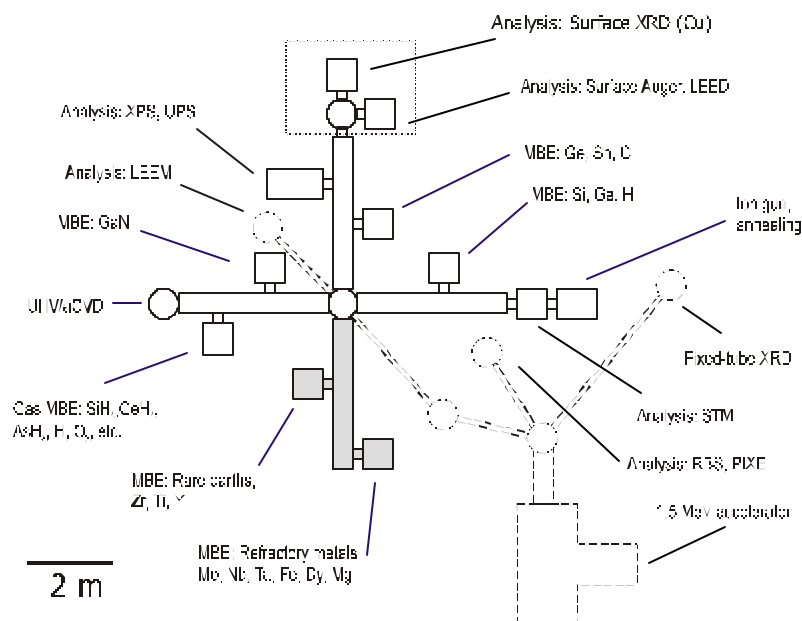


Figure 2.1. The Epicenter growth laboratory houses a variety of vacuum-interconnected thin film growth and characterization equipment. The shaded areas are the systems described in this thesis. The lower floor is shown as a broken line.

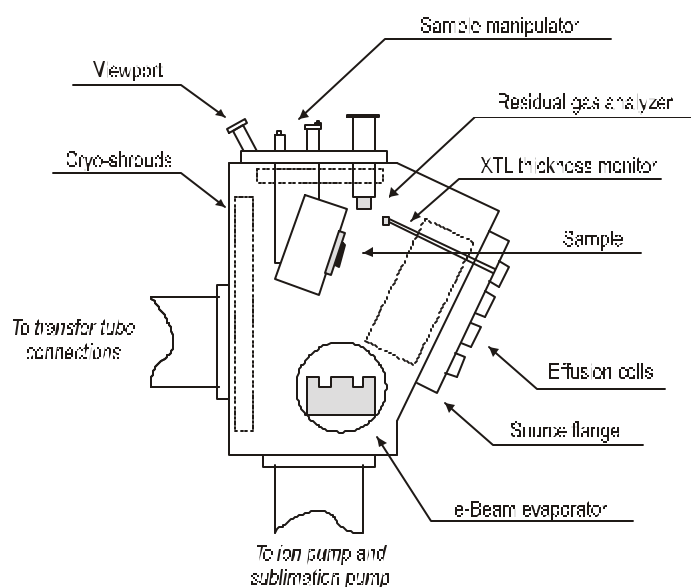


Figure 2.2. Cross-section of a Perkin-Elmer 430 MBE machine. Growth and thickness determining equipment is labeled.

In both growth chambers the growth rate was monitored using Inficon quartz crystal thickness (XTL) monitors, and calibrated residual gas analyzers positioned in the flux near

the sample. The detection arrangement is shown in Figure 2.2. For the growth of Ti/Zr and Y/Lu alloys the RGA proved essential in establishing and monitoring the ratio of the co-evaporants. Surface quality was verified with RHEED, as discussed below.

## 2.3 Surface Characterization

### Reflection High-Energy Electron Diffraction

The thin films synthesized in the present work comprise several layers. Structural imperfections in any one layer interfere with and may be amplified in subsequent layers, so it proved desirable for the surface structure of each layer to be carefully monitored during and subsequent to growth [2]. Reflection high-energy electron diffraction (RHEED) was therefore essential. In practice the conditions for the growth of Lu on Zr were continually readjusted, depending on the surface structure measured using RHEED.

In RHEED a focused beam of 10 keV - 100 keV electrons diffracts from a surface at grazing incidence, typically  $1^\circ$ , onto a phosphor screen [3],[4]. The Ewald construction in Figure 2.3 clarifies the origins of the diffraction pattern, but in practice data analysis is accomplished by comparison with the expected surface mesh [5]. If the crystal surface is a two-dimensional net with basis vectors  $\mathbf{a}_1$  and  $\mathbf{a}_2$ , the reciprocal space is a collection of infinite “rods” which form a lateral (in-plane) net,

$$\begin{aligned}\mathbf{a}_1^* &= 2\pi \mathbf{a}_2 \times \hat{\mathbf{n}} / A ; \\ \mathbf{a}_2^* &= 2\pi \mathbf{a}_1 \times \hat{\mathbf{n}} / A ,\end{aligned}\tag{2.1}$$

where  $A = \mathbf{a}_1 \cdot \mathbf{a}_2 \times \hat{\mathbf{n}}$ . The real space Figure 2.3 shows clearly that the observed diffraction pattern, the intersection of the surface rods with the Ewald sphere, is the projection of this net along one azimuth onto the phosphor screen.

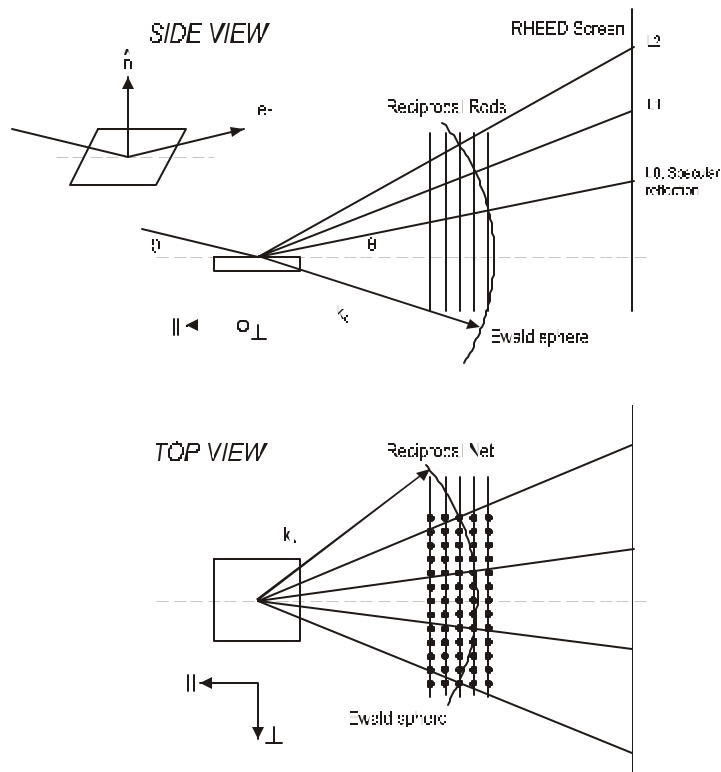


Figure 2.3. A schematic picture of a RHEED experiment, in which the Ewald sphere and Laue circles are indicated.

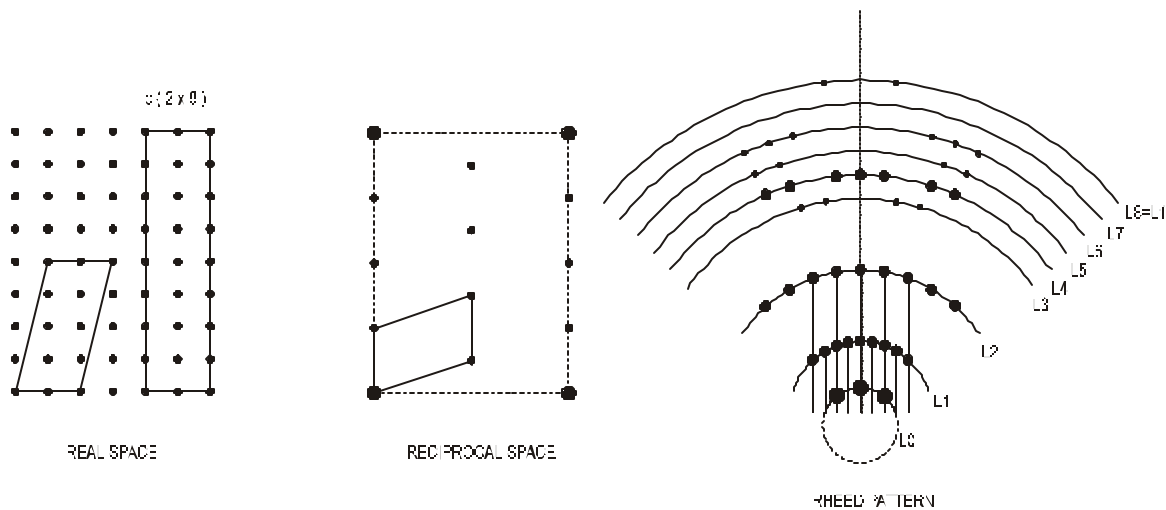


Figure 2.4. The connection between a surface unit cell and its diffraction pattern. Different reconstructions give identical diffraction patterns in the low-order Laue zone. The dashed lines are an ideal unit cell; the solid lines are the primitive and conventional unit cells of the reconstructed surface. After Reference [7].

Quantitative analysis of RHEED intensities is difficult. At these high electron energies, multiple scattering effects are important. Also, the observed diffraction pattern is a superposition of several effects, including surface resonance effects and diffraction from sub-surface atoms [6]. Fortunately, such detailed analysis is not needed to verify surface quality, since structural perfection is reflected in the sharpness of streaks and the degree of damping of higher-order Fourier components. In fact, refinement of Ta growth resulted in a RHEED pattern with at least four visible Laue circles, confirming that high structural perfection is possible when careful attention is given to the growth conditions.

Specific surface reconstructions observed on some buffer layers indicated that optimized growth conditions had been achieved. For example, optimally-grown Ta(211) has a  $3 \times 7$  reconstruction. Chapter 3 discusses these reconstructions. An important point, and one that is frequently overlooked, is that determination of the unit cell of the reconstruction involves careful analysis along several azimuths of higher-order Laue circles, not just the inter-streak separation at zero order [7]. The way in which a surface reconstruction is reflected in the RHEED pattern is shown in Figure 2.4.

A powerful application of RHEED is to identify (and, when used as feedback, to control) the epitaxial growth mode by monitoring the time-dependence of diffraction intensities. The diffraction intensity oscillates when the surface morphology changes periodically with thickness as monolayers are completed (for example, in a layer-by-layer growth mode). This process is shown in Figure 2.5. Chapter 3 presents RHEED oscillation data for the growth of Ti on Ta.

## Atomic Force Microscopy

Atomic force microscopy (AFM) was very useful in the refinement of growth conditions for b-axis-oriented rare earths. The instruments used included an Explorer (made by Topometrix, Inc.) and a Multi-Mode Nanoscope (made by Digital Instruments, Inc.). This Section first describes the technique, then discusses experimental errors, artifacts, and

necessary data correction schemes. Finally, useful measures of surface roughness are described.

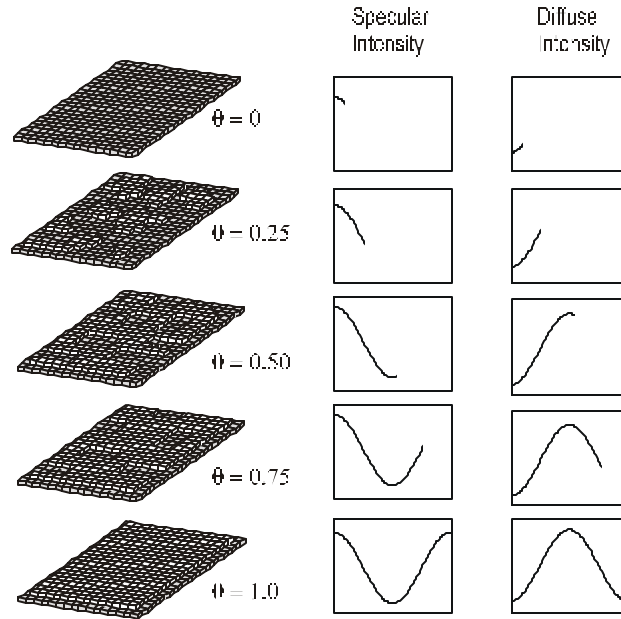


Figure 2.5. The origin of RHEED intensity oscillations. When the surface morphology is periodic, diffraction intensities oscillate with this same period (or with an integer multiple of this period).

AFM was developed in 1986 by Binnig, Quate, and Gerber [8]. Like the earlier scanning tunneling microscopy (STM), it is a scanning probe microscopy (SPM), in which a probe is scanned across a surface and its interactions with the surface recorded. Piezoelectric scanners with reproducible, sub-Angstrom positioning capability translate a sample under a probe “tip,” usually a shaped SiN wedge 100-500  $\mu\text{m}$  in length and several  $\mu\text{m}$  thick, fixed to a flexible cantilever. The cantilever deflection as the tip follows the surface is measured by laser reflection into a segmented photodiode array, as shown in Figure 2.6. Three-dimensional micrographs of surface topography (AFM) are obtained from the scanner correction needed to remove the tip/cantilever deflection. Micrographs of frictional and adhesive forces (lateral force microscopy, LFM) are similarly obtained from the measured cantilever torsion. Related techniques such magnetic force microscopy, STM, electric field microscopy, etc. are possible depending on the tip/surface interaction

[9]. More complicated scanning methods are also in use, including a tapping mode in which the amplitude of an oscillating tip is kept constant.

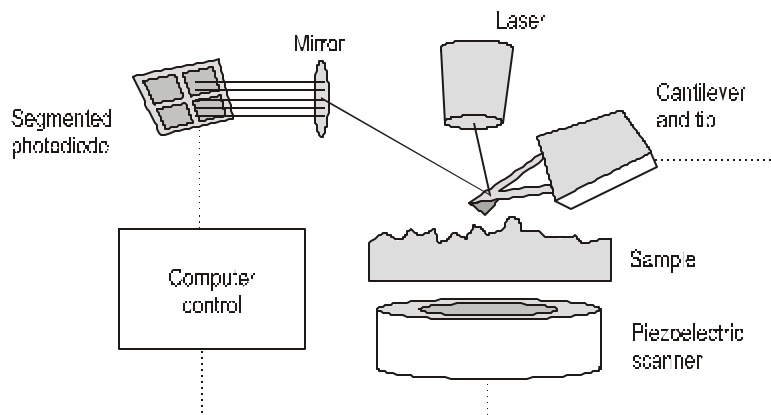


Figure 2.6. The principal elements of an atomic force microscope. Here the sample is translated by a piezoelectric scanner, but in some instruments the cantilever is translated.

A number of experimental artifacts involving the scanner, tip, laser, and sample must be avoided. A brief summary of these follows.

*Scanners.* Piezoelectric scanners are nonlinear and suffer from hysteresis and aging effects. The required corrections are made by the control software. Other scanner effects include *creep*, a slow drift after a sudden DC offset, identified by differences in micrographs collected at different rates; and *bow*, which is a nonlinear distortion at the edges of a long scan. A significant problem is establishing the proper feedback parameters for computer control of the scanner; when not optimal, AFM micrographs may look normal but do not properly describe the real morphology.

*Tips.* AFM micrographs are a convolution of tip structure with the real surface properties, so that deformation or non-sharpness of the tip cause significant effects. It is not possible to image features steeper than the tip angle, which is normally about 35°.

*Laser.* Reflection of laser light from shiny surfaces adds unwanted feedback to the control loop and is manifest in recognizable distortions of the images.

*Sample.* The sample can acquire a static electric charge. In the present work, all samples were “discharged” by brief exposure to a high-intensity radioactive polonium source prior to analysis. This is particularly important for insulating samples, such as sapphire. Most



surfaces contain physisorbed gases. The quality of the image depends significantly on the surface chemical state as well as its elastic compliance.

Some artifacts such as drift can be detected by inspection of the micrograph but many produce a surface topology which looks normal. For these reasons it is *essential* that AFM micrographs be collected under several measurement conditions to vary, when possible, the tip/surface angle, scan rate, and the direction of scan across the sample.

Several artifacts must be removed by post-processing. The sample cannot be leveled perfectly in the instrument so that a planar or higher order background surface must be subtracted. Also a scan across the sample may be randomly offset from adjacent scans, so a correction may be necessary (this was particularly important for the lower-quality Topometrix instruments). Further corrections such as filtering may also be needed.

Several methods for quantifying surface roughness are available. Scalar quantities such as mean-square-roughness are of limited utility for this purpose. For the example of two miscut surfaces, each perfectly flat except for different terrace heights, the AFM micrographs with the miscut angle subtracted will have surfaces with a “sawtooth” profile. The sample with larger miscut angle will then exhibit a larger rms roughness, despite the topology of both being identical except for terrace height. A widely-used approach for quantifying roughness is to compute the height-height or height-difference correlation function for the surface. This function contains information about the magnitude and length scale of roughness. Other, fractal measures can be employed, one of which, a lake-filling measure based on fractal dimensional analysis, is described in Chapter 3 [10].

## **2.4. Characterization of Bulk Properties**

### **Bulk Characterization by X-Ray Diffraction**

X-ray diffraction (XRD) proved to be the most useful means for determining structural properties of the samples grown in this work. This technique provides information about atomic periodicities and spatial coherence. Here the basic physics is first reviewed, and

then a mathematical description of scattering is presented. This is useful for both qualitatively and quantitatively interpreting x-ray measurements at high angles.

There are numerous techniques for thin film characterization using x-rays. The most common are *high-angle* x-ray diffraction and *low-angle* x-ray reflectivity; both techniques use incoherent, monochromatic radiation. In the high-angle regime, diffraction from structural periodicities gives rise to a continuous, weak distribution of diffracted intensity from diffuse scattering, crystal truncation, etc., separated by compact regions that contain the high intensity of Bragg peaks. In the low-angle regime, x-ray radiation refracts from layers with different refractive indices which comprise the sample, giving rise to a series of angle-dependent reflection maxima related to the sample composition.

The usual approach has been to consider these regimes separately. For high angles, the intensity  $I$  at momentum transfer  $\mathbf{q}$  is related to the modulus-squared of the structure factor  $F$ ,

$$\begin{aligned} F(\mathbf{q}) &= \sum_{\mathbf{r}} f_i \exp(i\mathbf{q} \cdot \mathbf{r}) ; \\ I(\mathbf{q}) &= \langle F(\mathbf{q}) F^*(\mathbf{q}) \rangle , \end{aligned} \tag{2.2}$$

where the sum is over the scatterers in the sample, and  $\langle \rangle$  denotes an average over fluctuations [11],[12]. For small angles, the scattering intensity can be calculated using an optical formalism with matrices [13],[14].

Miceli recently showed that the high- and low-angle regimes can be expressed as the limiting behavior of a unified formalism [15],[16]. This formalism provides a convenient means to understanding the shapes of Bragg reflections at high angles. The mathematical results are complex, but the result is that a Bragg reflection contains two components: a *narrow* component with an intensity that decays along  $\mathbf{Q}_\perp$  (the “Bragg scan” direction) as an exponential function of the in-plane atomic disorder; this derives from translational invariance obtained from registry with the substrate [17]; and a *broad* component, whose linewidth along  $\mathbf{Q}_\parallel$  (the “rocking curve” direction) depends on

whether the fluctuations in roughness saturate within the length of coherence probed by the x-rays [18],[19]. If the

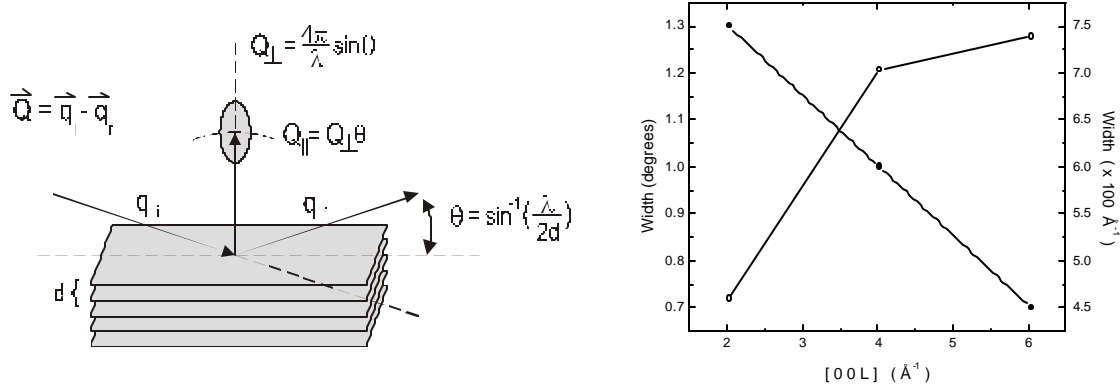


Figure 2.7. (Right) The scattering geometry for the first Bragg peak. (Left) Transverse x-ray linewidth of several Bragg reflections measured by angle (solid circles, left axis) and momentum transfer (open circles, right axis). This indicates roughness which is not described by the mosaic and coherence-limited models.

roughness has saturated, the linewidth  $\Delta Q_{\parallel}$  varies linearly as scattering angle  $\theta$  (mosaic limit); if instead the roughness limits the coherence,  $\Delta Q_{\parallel}$  depends on  $\sin(\theta)$  (coherence limit). Examples of both types of roughness in the same epitaxial system have been reported. Nb(110)/Al<sub>2</sub>O<sub>3</sub> samples grown by the author show mosaic disorder [22]; similar films studied by Gibaud et al. reveal finite-size disorder [23].

No two-component lineshape is observed in b-axis-oriented rare earths. The specular peak at large  $Q$  is strongly suppressed by disorder, and the transverse linewidth arises from mosaic. Interestingly, early b-axis-oriented Dy films, grown before an optimized procedure was developed, exhibit a transverse lineshape which is not adequately described by either regime. These data, presented as Figure 2.7, show a transverse linewidth for Dy which is not constant with either scattering angle or momentum transfer. This suggests the lineshape derives from roughness which differs from both the mosaic limited and coherence-length limited regimes.

## X-Ray Determination of Miscut Angle

It was recently found that the substrate miscut angle can influence the morphology of thin films grown on sapphire [24]. It was necessary to measure the miscut angle between the optical surface and the crystal axes of the sapphire wafers, both to verify substrate quality and to avoid possible complications when refining the b-axis-oriented rare earth growth process [25]. This Section first reviews the original method and then describes a new apparatus developed in this research for precise measurements of miscut angle, which has since been employed by other researchers.

The first apparatus employed to determine sample miscut was a Laue backscattering camera combined with laser alignment. The sample, mounted on a two-circle vernier goniometer, was positioned normal to a specific axis using a reflected laser spot as a guide. Next, a series of Laue backscattering photographs was taken, readjusting the goniometer as needed to align the crystal along the same normal axis. The miscut angle and direction could then be calculated from the change of goniometer settings. Since the central spot in a Laue backscattering photograph is not visible, each attempt at alignment required a double exposure of pictures taken 180° apart, to bring the off-center Laue spots into coincidence. Several alignment attempts were required. This technique worked adequately with 0.1° accuracy, but it was time-consuming and could be applied easily only to samples with two-fold Laue spot symmetry.

To implement a more user-friendly and widely-applicable approach, a phi-circle sample mount was designed for the Rigaku DMAX2 diffractometer. The sample was secured using green modeler's clay with its optical surface normal to the rotation axis; a laser could be used to verify the alignment. Next, a sequence of XRD "rocking" scans was performed, each at a different  $\phi$  but the same  $2\theta$  angle. Because this diffractometer uses line focus and collimation, the rocking scans measure the projection of the reflected spot into the diffraction plane [26]; that is,

$$q - (2q) / 2 = M \sin(f - f_0) \quad (2.3)$$

where  $M$  and  $f_0$  are the miscut magnitude and direction. The crystal miscut is then obtained by a simple analysis of  $\theta$  vs.  $\phi$ , as shown in Figure 2.8. A measurement of miscut and direction, accurate to better than  $0.1^\circ$ , requires about 15 minutes per sample.

Data analysis for this technique was studied in some detail, and it was found that the accuracy was not strongly affected by common systematic errors [27],[28]. These errors include misalignment of the x-ray beam or the sample from the center of the goniometer rotation axes. Interestingly, Eq. (2.3) was found as an approximation which differed negligibly from a considerably more complicated expression [27].

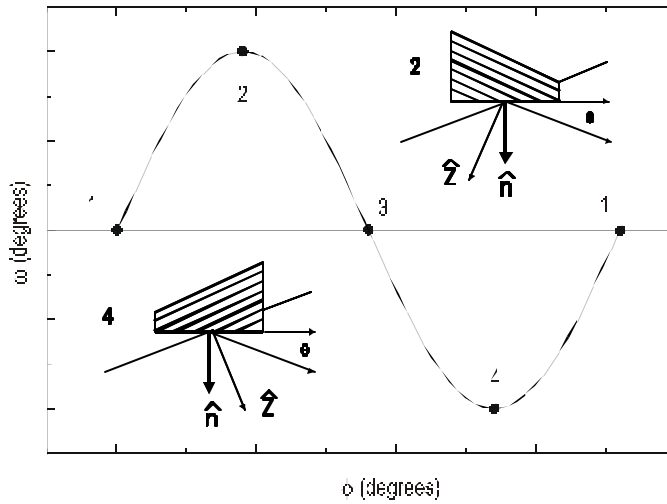


Figure 2.8. Schematic of sample miscut (magnitude and direction) determination using the Rigaku two-circle diffractometer and a new  $\phi$ -stage, discussed in the text.

## Pole Figure Measurements

In addition to measurements of miscut, the  $\phi$ -stage described in the last Section also facilitates x-ray pole figure measurements. A pole figure is a cross-section of reciprocal space,  $Q_x$  vs.  $Q_y$ , which gives information about in-plane structural order and periodicities [29]. Since these measurements are often performed on modified two-circle machines (as in the present case), care must be taken in interpreting the resulting data: each “slice” through this contour represents data collected with vertical slits and therefore is the projection of the actual three-dimensional x-ray spot onto the diffraction plane. In

contrast, a reciprocal space map, usually performed on a four-circle diffractometer with pinhole-type collimation and receiving slits, provides data in which each point represents the x-ray intensity collected at a specific location  $(Q_x, Q_y)$ , with a specific resolution function [30]. Pole figure measurements and further discussion are presented in Chapter 3.

## Backscattered Laue Photography

Backscattered Laue photography is a convenient technique for identification of the in-plane crystallography of substrates. The surface is placed normal to a collimated, non-monochromatic x-ray beam, and diffracted radiation is backscattered onto a phosphor screen in contact with photographic film. The beam is non-monochromatic and therefore contains many wavelengths which are able to diffract from most atomic plane spacings in the sample. The film records a spot pattern from which the in-plane crystallography can readily be determined. This technique is useful for thin films, when the film makes a negligible contribution or attenuation of substrate diffraction.

In general, Laue patterns are difficult to interpret and it is generally necessary to consult an authoritative text [31]. Since the substrates are sapphire, Figure 2.9 presents Laue photographs of the common orientations of this crystal, with the in-plane principal axes specified.

Figure 2.9. Laue photographs of the four principal orientations of sapphire, with the important in-plane directions specified. The photographs have been enhanced for maximum clarity.

## Rutherford Backscattering Spectroscopy

Rutherford backscattering spectroscopy (RBS) is indispensable for accurate thickness measurements and to provide information about the composition of thin films, including interdiffusion. This technique has been treated in several theses, review articles and books

[32]. This Section addresses salient aspects of this technique which were invaluable to this research. In particular, a new method of RBS data analysis is described.

In RBS a beam of  $^4\text{He}$  nuclei (typically 0.5 - 3 MeV) is directed into a material, from which it backscatters inelastically. The backscattered energy distribution is measured by means of Si surface barrier detector. The process of implantation, scattering, and backscattering is well-described by a model in which the  $^4\text{He}$  nuclei lose kinetic energy as they travel through the medium and undergo occasional elastic scattering events which change their direction [32].

A key point concerning RBS data analysis concerns three distinct procedures for data analysis to extract the abundance of a given element (termed the “coverage” of atoms/area). Like the phase problem in x-ray diffraction, the “inverse RBS problem” is not solvable in general; that is, given an experimental backscattered energy distribution, there is no analytical method to directly obtain the structure. The three methods of data analysis outlined here are facilitated by commercial software [33].

*1. Direct integration.* If the peak from a given element species in a backscattered energy spectrum is well-resolved, or if a reasonable estimate of the peak shape can be made, then the peak area can be obtained by integration to yield the material coverage by species immediately. The coverage  $N$  is related to the yield  $Y$  by

$$Y = Q \cdot N \cdot \frac{dS}{d\Omega}, \quad (2.4)$$

where the Rutherford differential cross section is

$$\frac{dS}{d\Omega} = \left( \frac{Z_1 Z_2 e^2}{2E} \right)^2 \frac{\left[ 1 - M_1^2 \sin^2 \theta / M_2^2 \right]^{1/2} + \cos \theta}{\left[ 1 - M_1^2 \sin^2 \theta / M_2^2 \right]^{1/2} \sin^4 \theta}. \quad (2.5)$$

Here  $d\Omega$  is the solid angle of the detector,  $Q$  is the fluence, and  $M_1, M_2$  and  $Z_1, Z_2$  are the mass and atomic numbers of the  $^4\text{He}$  projectile and target atom, respectively.

2. *Peak area ratios.* If one desires only an assessment of *relative* concentrations, such as the ratio of Cu to Au in a Cu<sub>3</sub>Au compound, and if the peaks are sufficiently well-resolved, then the charge and detector solid angle need not be measured. The ratio of coverages is related to the ratio of the yields by

$$\frac{Y_A}{Y_B} = \left( \frac{ds}{d\Omega} \right)_A / \left( \frac{ds}{d\Omega} \right)_B \cdot \frac{N_A}{N_B} \quad (2.6)$$

3. *Profile fitting.* It often happens that a peak cannot be directly integrated, due to its overlap with neighboring peaks. These cases require that the spectrum be compared with the spectrum calculated from a model structure. The parameters of the model are adjusted until a good fit is obtained. In spectra from b-axis-oriented samples the peaks are superposed and integration is impossible, so the coverages must be estimated in this way from a simulation.

A new method developed by N. Barradas at the University of Surrey and employed by the author in collaboration circumvents many difficulties of nonlinear fitting [34]. This method involves simulated annealing to optimize fits for systems with many degrees of freedom. The only initial conditions specified are the elements which compose the sample, and a robust fitting procedure then determines the thickness and location of each layer. Figure 2.10 compares the best fit using traditional analysis software with an improved fit using simulated annealing. The analysis reveals that the Zr and Ti buffer layers coexist to a depth of about 250 at/cm<sup>2</sup>, an impressive result since the alloying of these elements is not an initial condition. More precise characterization is impossible, however, due to the energy resolution and also the additional effects of multiple scattering and straggling, not



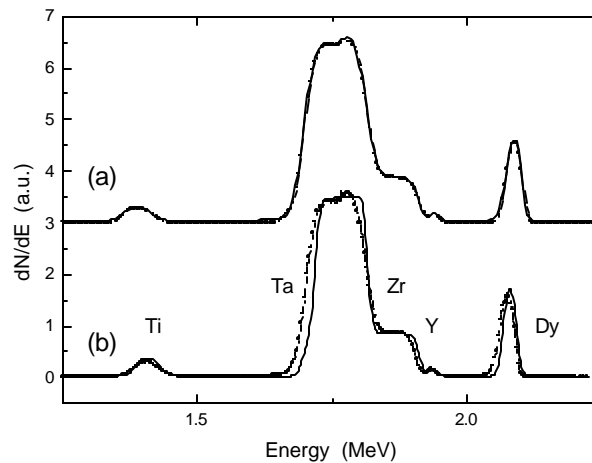


Figure 2.10. Comparison of data analysis schemes for RBS. (a) A fit using the simulated annealing method. (b) A fit by hand using the conventional RUMP program. In this case, fitting by hand is difficult because b-axis-oriented rare earths contain composition-graded layers and alternating heavy and light metals. After Reference [34].

included in the simulation. Such characterization is possible in principle, however; using advanced detection apparatus one can even resolve isotopic distributions.

## 2.5 Measurement of Magnetic Properties

### SQUID Magnetometry

Magnetic properties were determined using the 1 T and 7 T SQUID magnetometers of the University of Illinois Magnetic Characterization Facility. These magnetometers (made by Quantum Designs, Inc.) can measure total moments as low as  $10^{-7}$  emu. This is much smaller than the typical  $10^{-6}$  to  $10^{-3}$  emu moments of b-axis-oriented Dy samples. The operation of the magnetometers is discussed fully in Reference [35]. Here the measurements are first described, and then the data processing is addressed.

The magnetic field of a sample is determined indirectly from the electric current it induces as it passes longitudinally through a single, superconducting wire wound into a second-derivative, three-coil arrangement, as shown inset in Figure 2.12. This arrangement

eliminates detection noise caused by fluctuations of the superconducting magnet. The induced current is converted to a voltage by a shielded, high-sensitivity SQUID detector, and this is fitted to a simple model of a dipole of strength  $A$  passing through current loops of radius  $R$  separated by a distance  $\Lambda$ ,

$$V(z) = c_1 + c_2 z + \frac{A}{R} \times \left\{ \frac{2}{R^2 + (z + z_0)^{3/2}} - \frac{1}{\left[ R^2 + (\Lambda + z + z_0)^2 \right]^{3/2}} - \frac{1}{\left[ R^2 + (-\Lambda + z + z_0)^2 \right]^{3/2}} \right\}, \quad (2.7)$$

where  $c_1$  and  $c_2$  are calibration factors, and  $z_0$  is a (possible) offset along the magnet axis. This analysis is performed by software provided with the instrument.

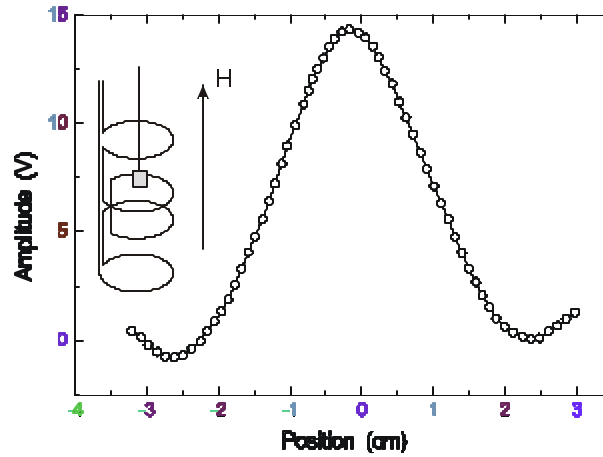


Figure 2.11. The SQUID signal as the sample is passed through the detection coils. The sample moment is determined by fitting these data to a simple model (see text). The insert shows the sample, the second-order gradiometer coil, and the applied field.

## Sample Preparation

Prior to measurement the samples were cleaned using a precision bead-blaster to remove the unwanted ceramic adhesive from the sapphire. Next, the in-plane crystallography was determined by Laue backscattering. Then, using a diamond-impregnated wafering blade the sample was sectioned into rectangular shape, typically 0.5 x 0.5 cm. The initial pre-cutting of the substrates into crystallographically-aligned rectangular samples, and the

frequent presence of one or more ultrathin “slip” lines across the surface of the sample parallel to the (0001) plane of sapphire (see Chapter 3), made this task easy.

The sample was then placed into a cotton-filled section of a soda straw, and inserted into a long soda straw fixed to the end of the sample rod. Precise location of the sample within the straw at exactly 9.5 cm from the bottom end was important so that spurious edge effects due to proximity of the straw ends to the detection coils were minimized. As cotton contains inhomogeneous magnetic impurities, the same cotton was used for successive measurements so that the background signal could easily be measured and subtracted, as discussed below.

## Data Reduction and Analysis

An example of a measured hysteresis loop for a Dy film with  $\epsilon_{11}=-1.36\%$  is shown in Figure 2.12. Here the raw magnetic signal of the Dy sample is superimposed on several unwanted background contributions which include 1) the diamagnetic background from the sapphire substrate, the soda straw, and the cotton; 2) a ferromagnetic background from a magnetic impurity in the Zr buffer layer; 3) a paramagnetic background from the non-RE metallic buffer layers, which was small and could be ignored. These parasitic contributions were removed in the following way: *Diamagnetic subtraction.* The sapphire, straw, and cotton were each measured separately, and then the diamagnetic signal subtracted [36]. *Ferromagnetic subtraction.* The FM background from a sample containing only Zr was measured. The signal was independent of temperature in the region of interest, and was well-fit by an empirical expression

$$M = M_0 \left[ 1 - 2(1 + \exp(ax))^{-1} \right]. \quad (2.8)$$

By fitting Eq. (2.8) to a hysteresis loop in the paramagnetic region of Dy,  $M_0$  and  $a$  were determined; the resulting expression of Eq. (2.8) was subtracted from all other hysteresis loops. Note that the FM background saturates and it is therefore easily subtracted from the

hysteresis loops, but extraction from ZFC/FC curves in small aligning fields (500 Oe) is not possible.

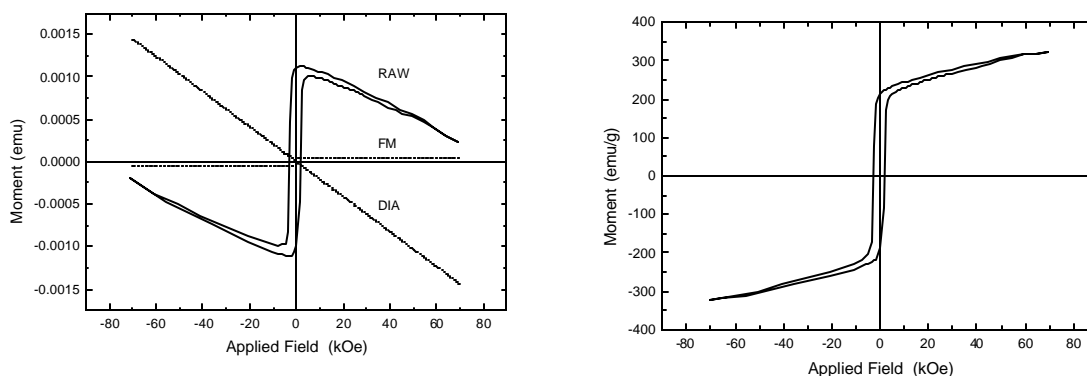


Figure 2.12. (Left) A measured hysteresis loop for a Dy sample with  $\epsilon_{11}=-1.36\%$ , with the diamagnetic and ferromagnetic backgrounds shown. (Right) The same hysteresis loop after the background corrections have been made.

## References

- [1] D. H. Hennison, M. J. Tschueeter, K. A. Gschneidner, *J. Less-Common Metals*, **11**, 423-435 (1966).
- [2] RHEED could not be performed during Ta and Zr growth. Light emitted from the molten source material saturated the phosphor screen. In addition, the electromagnetic raster of the evaporator interfered with the RHEED beam.
- [3] Typically, this is a Cu-doped zinc sulphide compound. A P31 phosphor (GTE) was used in the present research. See *Inorganic phosphors and related chemicals* (GTE Products Corp., Towanda, PA, 1990).
- [4] For a general discussion about phosphors, see I. D. Csorba, *Image tubes* (Sams, Indianapolis, 1990) and references therein.
- [5] J. E. Mahan, K. M. Geib, G. Y. Robinson, R. G. Long, *J. Vac. Sci. Technol. A* **8**, 3692-3700.
- [6] S. Bonham, Ph.D. thesis, University of Illinois, 1997.
- [7] I. Hernandez-Calderon, H. Höchst, *Phys. Rev. B* **27**, 4961-4965 (1983).

- [8] G. Binning, C.F. Quate, C. Gerber, *Phys. Rev. Lett.* **56**, 930-933 (1986).
- [9] G. Binnig, H. Rohrer, Ch. Gerber, W. Weibel, *Phys. Rev. Lett.* **49**, 57-61 (1982).
- [10] J. C. Russ, *Fractal surfaces* (Plenum, New York, 1994).
- [11] E. E. Fullerton, I. K. Schuller, H. Vanderstraeten, Y. Bruynseraede, *Phys. Rev. B* **45**, 9292 (1992).
- [12] H. Homma, S. Szpala, M. K. Sanyal, S. K. Sinha, S. K. Satija, C. F. Majkrzak, D. A. Neumann, H. Morkoc, *Physica B* **198**, 72-77 (1994).
- [13] J. Penfold, R. K. Thomas, *J. Phys. Condens. Matt.* **2**, 1369-1412 (1990).
- [14] E. E. Fullerton, I. K. Schuller, H. Vanderstraeten, Y. Bruynseraede, *Phys. Rev. B* **45**, 9292 (1992); E. E. Fullerton, J. Guimpel, O. Nakamura, I. K. Schuller, *Phys. Rev. Lett.* **69**, 2859 (1992); E. E. Fullerton, J. Pearson, C. H. Showers, S. D. Bader, X. Z. Wu, and S. K. Sinha, *Phys. Rev. B* **48**, 17432 (1993).
- [15] This approach was first applied in S. K. Sinha, E. B. Sirota, S. Garoff, H. B. Stanley, *Phys. Rev. B* **38**, 2297 (1988).
- [16] P. F. Miceli, *Semiconductor interfaces* (Hilger, Bristol, 1992).
- [17] J. D. Jackson, *Classical electrodynamics* (Wiley, New York, 1975).
- [18] P. F. Miceli, C. J. Palmstrom, K. W. Moyers, *App. Phys. Lett.* **58**, 1602-1604 (1992).
- [19] P. F. Miceli, C. J. Palmstrom, K. W. Moyers, *App. Phys. Lett.* **61**, 2060-2062 (1992).
- [20] P. F. Miceli, J. Weatherwax, T. Krentsel, C. J. Palmstrom, *Physica B* **221**, 230-234 (1996).
- [21] P. F. Miceli, C. J. Palmstrom, *Phys. Rev. B* **51**, 5506-5509 (1995).
- [22] P. M. Reimer, H. Zabel, J. A. Dura, K. Ritley, C. P. Flynn, *Z. Phys. Chem.* **181**, 375-80 (1993)
- [23] A. Gibaud, R. A. Cowley, D. F. McMorrow, R. C. C. Ward, M. R. Wells, *Phys. Rev. B* **48**, 14463 (1993).
- [24] G. L. Zhou, S. Bonham, C. P. Flynn, *J. Phys. Condens. Matt.* **9**, L671-L676 (1997).

[25] Subsequently a large collection of wafers was acquired, each with the same low miscut angle, thereby eliminating miscut as a possible random variable.

[26] H. Zhang, S. K. Satija, P. D. Gallagher, J. A. Dura, K. Ritley, C. P. Flynn, and J. F. Ankner, *Phys. Rev. B* **52**, 17501-17508 (1995).

[27] C. Durfee, private communication.

[28] M. Conover, private communication.

[29] P.F. Fewster, N. Andrew, *J. Phys. D App. Phys.* **28**, A97-A103 (1995).

[30] P. F. Fewster, *Rep. Prog. Phys.* **59**, 1339-1407 (1996).

[31] E. Preuss, B. Krah-Urban, R. Butz, *Laue atlas* (Wiley, New York, 1974).

[32] W. K. Chu, *Backscattering spectrometry* (Academic, New York, 1978).

[33] L. R. Doolittle, *Nuc. Instr. Meth. Phys. Res.* **B** 15, 227-231 (1986); L. R. Doolittle, *Nuc. Instr. Meth. Phys. Res. B* **9**, 344-351 (1985).

[34] N. Barradas, "Simulated annealing analysis of a complicated spectrum belonging to K. Ritley," Surrey University Ion Beam Facility, internal report, May 1997.

[35] M. McElfresh, *Fundamentals of magnetism and magnetic measurements* (Quantum Designs, San Diego, 1994).

[36] A bare sapphire sample was measured to determine the field-dependent susceptibility. This susceptibility ( $1.38 \times 10^{-6}$  emu/G/cm<sup>3</sup>) is used as a background correction because the mass of the sapphire in each sample is easily measured.